PHYSICAL REVIEW C **70**, 014306 (2004)

γ-ray spectroscopy of core-excited states in ^{51}Mn

J. Ekman, D. Rudolph, C. Andreoiu,* C. Fahlander, and M. N. Mineva
Department of Physics, Lund University, S-22100 Lund, Sweden

M. A. Bentley and S. J. Williams†
School of Chemistry and Physics, Keele University, Keele, Staffordshire, ST5 5BG, United Kingdom

R. Charity, E. Ideguchi,‡ W. Reviol, D. G. Sarantites, and V. Tomov
Chemistry Department, Washington University, St. Louis, Missouri 63130, USA

R. M. Clark, M. Cromaz, P. Fallon, and A. O. Macchiavelli
Nuclear Science Division, Lawrence Berkeley National Laboratory, Berkeley, California 94720, USA

M. P. Carpenter and D. Seweryniak
Physics Division, Argonne National Laboratory, Argonne, Illinois 60439, USA

(Received 13 April 2004; published 13 July 2004)

The level scheme of ^{51}Mn has been investigated using the ^{28}Si$(^{32}\mathrm{S},2\alpha 1p)^{51}$Mn fusion-evaporation reaction at 125 MeV beam energy. The γ rays were detected in the Ge-detector array Gammasphere, which was coupled to the 4π-charged-particle detector Microball and the Neutron Shell for the coincident detection of evaporated particles. Over 100 new γ-ray transitions connecting some 50 excited states have been identified. Most of the states are built on particle-hole excitations across the shell gaps at particle number $N=Z=28$. The rich experimental data allows for a comprehensive comparison of core-excited states with results from large-scale shell-model calculations, which are known to provide excellent predictions for the lower-lying yrast and near-yrast levels in $1f_{7/2}$ nuclei.

DOI: 10.1103/PhysRevC.70.014306 PACS number(s): 21.60.Cs, 23.20.En, 23.20.Lv, 27.40.+z

I. INTRODUCTION

Nuclei in the $1f_{7/2}$ shell, located between the doubly magic $N=Z$ nuclei ^{40}Ca and ^{56}Ni, offer a multitude of phenomena to be studied. Low-lying states in nuclei, in the vicinity of ^{40}Ca and ^{56}Ni, are well described by spherical shell-model calculations. However, ^{56}Ni was found to be a rather soft core, manifested experimentally by the relatively low excitation energy of the first 2^+ state and the relatively large $B(E2;2^+\rightarrow 0^+)$ value. This is reflected in Monte Carlo shell-model calculations, which reveal a closed core part of only 49% for the ground-state wave function of ^{56}Ni, along with a dominance of $1f_{7/2}-2p_{3/2}$ quadrupole correlations in the remaining part of the wave function [1]. A similar result is obtained using large-scale shell-model calculations [2]. $N\sim Z$ nuclei near the center of the shell, for example ^{48}Cr, exhibit a rotational behavior based on a significant ground-state deformation of $\beta_2 \gtrsim 0.3$ [3–5]. The experimentally observed interplay between single-particle and collective modes of excitation as a function of E_x and I can be reproduced in detail by modern large-scale shell-model calculations using the full fp model space [6]. This makes nuclei in the $1f_{7/2}$ shell one of the best understood regions in the nuclidic chart, and allows for sophisticated and subtle studies of isospin symmetry [7–13] and influence of isospin $T=0$ neutron-proton pairing on the structure of these nuclei [14,15].

Typically, the high-spin spectroscopy of nuclei in the $1f_{7/2}$ shell is established up to noncollective oblate or spherical terminating states, which have spins given either by the number of aligned $1f_{7/2}$ particles relative to ^{40}Ca, or by the number of aligned $1f_{7/2}$ holes with respect to ^{56}Ni [16]. More recently, a few levels beyond these terminating states could be identified in heavier $1f_{7/2}$ nuclei. They appear to be of a spherical nature, and the main components of their wave functions comprise particles in the upper fp shell, i.e., the $2p_{3/2}$, $1f_{5/2}$, and $2p_{1/2}$ orbits above the shell gap at $N,Z=28$ [17,18]. In this work we provide evidence for core-excited states in the nucleus $^{51}_{25}$Mn$_{26}$. The amount and quality of information in ^{51}Mn allows for a rigorous test of large-scale shell-model calculations for this class of states. Such a comparison can form the basis for subsequent studies of, for example, mirror nuclei involving core-excited states.

In the course of previous high-spin investigations of ^{51}Mn [13,19–21], the $I^\pi=27/2^-$ terminating state has been reached, for which the angular momenta of the five $1f_{7/2}$ holes relative to the ^{56}Ni core are completely aligned. Spins and parities for the states up to the terminating state have been determined. The $17/2^-$ state has been found to be a nanosecond isomer [13,22]. In a recent publication, a rotational band was identified at high angular momentum in ^{51}Mn [23]. The configuration of the band involves one neu-

---

*Present address: Department of Physics, University of Guelph, Guelph, Ontario, Canada NIG 2W1.

†Present address: School of Chemistry and Physics, University of Surrey, Guildford, Surrey GU2 7XH, United Kingdom.

‡Present address: RIKEN, Saitama 351-0198, Japan.

tron in the $1g_{9/2}$ intruder orbit, which makes ^{51}Mn the lightest nucleus where in a collective structure based on a $1g_{9/2}$ particle has been observed.

II. EXPERIMENT AND DATA ANALYSIS

The present work is based on data from two experiments. The first experiment was performed in 1999 at Argonne National Laboratory (ANL), using the Argonne Tandem-Linac Accelerator System. The second experiment was performed at the Lawrence Berkeley National Laboratory (LBNL), using the 88-in. cyclotron. Both experiments employed the $^{28}\mathrm{Si}(^{32}\mathrm{S},2\alpha 1p)^{51}\mathrm{Mn}$ fusion-evaporation reaction at a beam energy of 125 MeV. The ^{28}Si targets were enriched to 99.90% and had a thickness of 0.5 $\mathrm{mg/cm^2}$. They were supported with a 1 $\mathrm{mg/cm^2}$ Au and Ta foil, respectively, in both experiments. In addition, part of the LBNL experiment was performed using a 13 $\mathrm{mg/cm^2}$ Ta backing. The γ rays were detected in the Gammasphere array [24], which comprised 78 Ge detectors. The Heavimet collimators were removed to allow for γ-ray multiplicity and sum-energy measurements [25]. For the detection of light charged particles the 4π-CsI-array Microball [26] was used. To discriminate weak reaction channels at or beyond the $N=Z$ line, evaporated neutrons were measured in the Neutron Shell [27], which replaced the 30 Ge detectors at the most forward angles. Events with four or more Ge detectors in coincidence were written to magnetic tape. At the end of the experiments data were taken with ^{56}Co, ^{133}Ba, and ^{152}Eu standard sources to calibrate the Ge detectors.

To obtain clean particle gated spectra with sufficient statistics, the discrimination between protons and α particles is of great importance. Each Microball event was associated with time, energy, and charge-ratio signals, where the latter was obtained using pulse-shape techniques [26]. These signals were plotted in different combinations in three two-dimensional spectra. Particles were identified only after fulfilling gate conditions in all three maps [28]. The obtained proton and α efficiencies were $\epsilon_p \sim 65\%$ and $\epsilon_\alpha \sim 50\%$, respectively, in these experiments.

To improve the γ-energy resolution, an event-by-event kinematic reconstruction method was applied to reduce the effect of the Doppler broadening caused by the evaporated particles. This is particularly important for reaction channels populated via α-particle emission, such as ^{51}Mn, since the γ-ray energy resolution is improved by ~40% for transitions originating from ^{51}Mn.

^{51}Mn was populated in the $2\alpha 1p$ reaction channel, which was found to account for about 18% of the total experimental fusion cross section by investigating the normalized yields of ground-state transitions in particle-gated E_γ projections. In fact, it was the strongest reaction channel. In the analysis, E_γ projections and E_γ-E_γ-E_γ cubes in coincidence with two α particles and one proton, and E_γ-E_γ matrices in coincidence with two α particles and one proton or two α particles, were used. Their examination employed the RADWARE software package and the spectrum-analysis code TV [29,30]. To study certain regions in the excitation scheme the E_γ-E_γ matrices were eventually obtained in coincidence with selected γ-ray transitions. Contaminating transitions arose mainly from the $2\alpha 2p$ channel, when a proton escaped detection, and from the 3α channel when an α particle escaped detection. These contaminants were suppressed by applying the total-energy plane selection method [31], and the remainders were subtracted from the $2\alpha 1p$-gated E_γ spectra.

Multipolarity assignments of γ-ray transitions were based on two methods. In both cases the 78 Ge detectors of Gammasphere were grouped into four "pseudo" rings corresponding to average angles $\overline{\theta}=30°$ (15 detectors), $\overline{\theta}=53°$ (15 detectors), $\overline{\theta}=70°$ (20 detectors), and $\overline{\theta}=83°$ (28 detectors). The efficiency-corrected intensity ratios of γ-ray transitions in the $\overline{\theta}=30°$ ring over the $\overline{\theta}=83°$ ring, R_{30-83}, were deduced. In most cases, R_{30-83} was determined from γ-ray spectra in coincidence with a proper subset of transitions from ^{51}Mn. Coincidences with transitions detected at an average angle $\overline{\theta}=56°$, where the relative intensities from different multipolarities are roughly the same, were required and spectra were projected out at $\overline{\theta}=30°$ and $\overline{\theta}=83°$. Stretched $E2$ transitions are predicted to have $R_{30-83}\approx 1.2$, whereas stretched $\Delta=1$ transitions should have $R_{30-83}\approx 0.8$.

Directional correlations of oriented states (DCO ratios) defined as

$$R_{\mathrm{DCO}}(30-83;\gamma_1,\gamma_2)=\frac{I(\gamma_1 \text{ at } 30°;\text{gated with } \gamma_2 \text{ at } 83°)}{I(\gamma_1 \text{ at } 83°;\text{gated with } \gamma_2 \text{ at } 30°)}, \tag{1}$$

were also deduced. The DCO ratios $R_{\mathrm{DCO}}(30-53)$ and $R_{\mathrm{DCO}}(53-83)$ are defined accordingly. Known stretched $E2$ transitions were used for gating, and in this case, we expect $R_{\mathrm{DCO}}=1.0$ for observed stretched $E2$ transitions for all three ratios. Stretched $\Delta I=1$ transitions should have $R_{\mathrm{DCO}}(30-83)\approx 0.6$, whereas ≈ 0.8 is expected for the other combinations.

In a few cases, efficiency-corrected intensities from γ-ray spectra in coincidence with two α particles and one proton detected between 70° and 163° were used to obtain angular distributions. The angular distributions, together with DCO ratios, were used to extract experimental mixing ratios, $\delta(E2/M1)$, for several transitions. An example is presented in the next section.

The alignment coefficient, α_2, and its uncertainty, $\Delta\alpha_2$, was usually calculated according to the empirically obtained estimate,

$$\alpha_2 = 0.55 + 0.02E_x(\mathrm{MeV}),\quad \Delta\alpha_2 = \pm 0.05, \tag{2}$$

which has proven to work well on nuclei in the fp shell [18,32].

III. RESULTS

Figure 1 shows the deduced level scheme from this work. Assignments of new transitions and their location in the level scheme are based on $\gamma\gamma$ and $\gamma\gamma\gamma$ coincidences, relative intensities, and sum-energy relations of transitions. Spin and parity assignments are based on DCO ratios and R_{30-83}

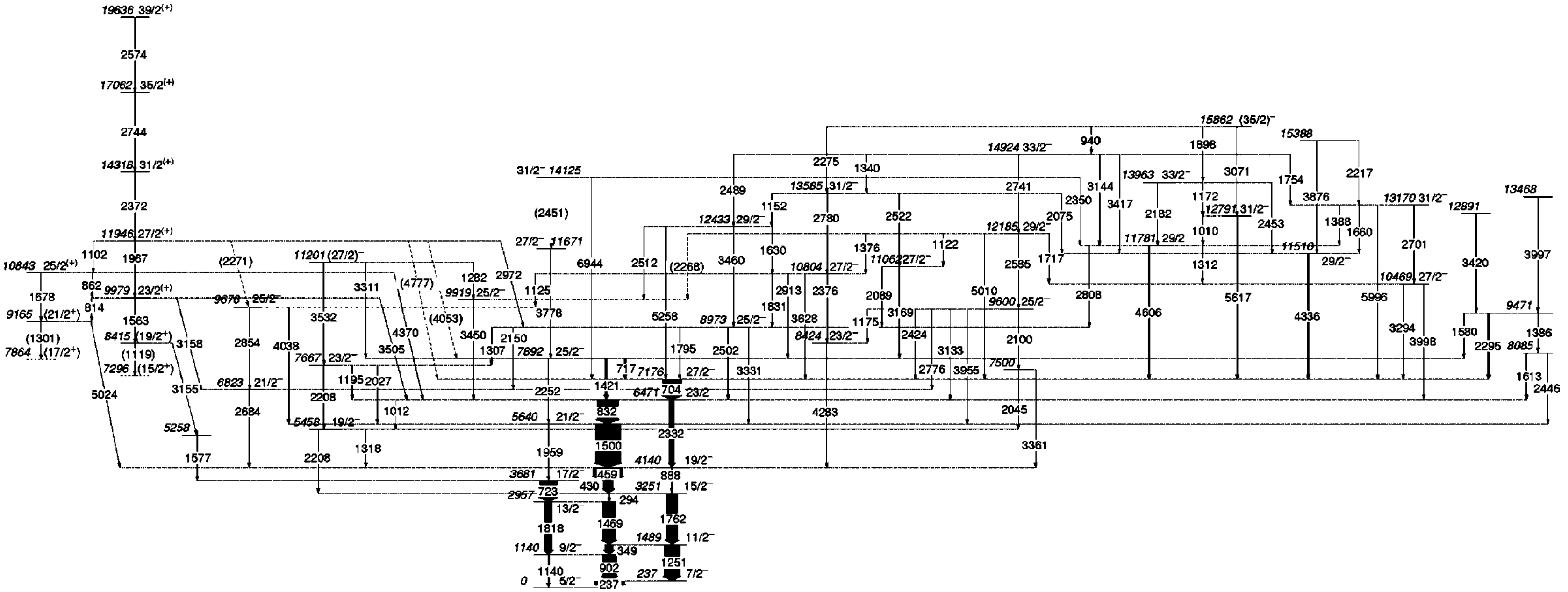

FIG. 1. The proposed level scheme of ^{51}Mn. Energy labels are in keV, tentative transitions and levels are dashed, and the widths of the arrows correspond to the relative intensities of the transitions.

values in Table I. On the left-hand side of Fig. 1, a previously identified rotational structure is seen [23].

Several high-energy γ-ray transitions are included in the level scheme, which connect $29/2^-$ and $31/2^-$ states with the previously known yrast 7176 keV $27/2^-$ state. Figure 2(a) shows the high-energy part of the γ-ray spectrum in coincidence with several strong transitions below the yrast $27/2^-$ state from a $\gamma\gamma$ matrix gated with two α particles and one proton. In the figure peaks at $E_\gamma=4336$, 4606, 5010, 5258, 5617, 5996, and 6944 keV are seen together with some of the respective single-escape peaks at $E_\gamma-511$ keV. The 5617, 5996, and 6944 keV transitions are assigned to stretched $E2$ transitions by the R_{30-83} and DCO ratios given in Table I. Figure 2(b) shows the γ-ray spectrum in coincidence with the $31/2^-_1\to 27/2^-_1$ 5617 keV transition. It is coincident with the $27/2^-_1\to 23/2^-_1$ 704 keV transition, as well as with the other transitions belonging to the low-energy yrast structure. In addition, peaks at $E_\gamma=1171$, 1898, and 3071 keV are seen, representing two parallel decay branches which connect the yrast $35/2^-$ and $31/2^-$ states. Gating on the other high-energy transitions in Fig. 2(a) reveal similar coincidence patterns. R_{30-83} and DCO ratios support dominant stretched $M1$ character for 4606, 5010, and 5258 keV transitions, whereas they would, at first glance, suggest an $E2$ assignment for the 4336 keV transition. However, a detailed DCO ratio and angular-distribution analysis presented in Fig. 3 shows that the 4336 keV transition is a mixed $\Delta I=1$ $E2/M1$ transition with a pronounced negative mixing ratio.

In the analysis, special care has been taken in the choice of the alignment coefficient when extracting mixing ratios from a DCO-ratio analysis, if using the 704 keV $27/2^-\to 23/2^-$ transition as the gating transition in Eq. (1). This is exemplified in the following discussion. The evaporation of particles and subsequent γ-ray decays partly destroy the initial spin alignment in the reaction plane. This is represented by an alignment coefficient, α_2, which is smaller than unity, and these effects are approximately taken into account by using Eq. (2). However, long-lived states will decrease the alignment coefficient further. Such an effect is present in most of the DCO ratios in Table I, since they are obtained in coincidence with the stretched 704 keV $E2$ transition depopulating the long-lived, $\tau=101(4)$ ps [33], yrast $27/2^-$ state. This is seen when comparing the alignment coefficient $\alpha_2=0.57$ extracted from an angular distribution of the 704 keV transition, with $\alpha_2=0.69$ calculated from Eq. (2). After correcting for this additional dealignment, consistent mixing ratios were obtained for all three DCO ratios in Fig. 3. The same correction is made when extracting $\delta(E2/M1)$ from the DCO ratios where the 704 kev transition has been used for gating. Based on this discussion it is clear that R_{30-83} ratios, DCO ratios, and angular distributions for transitions below the yrast $\tau=2.07\binom{8}{7}$ ns $17/2^-$ state are not very useful. However, for completeness R_{30-83} and DCO ratios for these transitions are still given in Table I.

Figure 4 shows a selection of spectra deduced from $\gamma\gamma$ matrices gated on two α particles and one proton, and several strong transitions below the yrast $27/2^-$ state. Panels (a) and (b) are the spectra obtained after requiring a coincidence with the $29/2^-_1\to 27/2^-_1$ 4336 keV and the $29/2^-_2\to 27/2^-_1$ 4606 keV high-energy transitions, respectively. In panel (a) several peaks corresponding to transitions belonging to the well-known low-energy structure are seen, but other lines are also visible. The peak at 1660 keV is assigned to the $31/2^-_2\to 29/2^-_1$ decay. It is interesting to note that no obvious coincidence with a possible 1281 keV $31/2^-_1\to 29/2^-_1$ transition is observed. The peak at 2453 keV marks the connection to the yrast $33/2^-$ state, whereas the 2075 and 3417 keV peaks represent the decays of nonyrast $31/2^-$ and $33/2^-$ states, respectively. In panel (b) a line at 2182 keV is visible and is assigned to the $33/2^-_1\to 29/2^-_2$ branch. On the right shoulder of the 2332 keV peak a line at 2350 keV is seen, which marks the decay of the 14125 keV $31/2^-_4$ state. The very same state decays to the yrast $27/2^-$ state via the emission of a 6944 keV transition highlighted in the inset of Fig 2. In panel (b) a line at 3144 keV is also obvious, which corresponds to the decay of the $33/2^-_2$ state. A peak at the same energy and representing the same transition is also visible in panel (c), which is the spectrum in coincidence with the $35/2^-_1\to 33/2^-_2$ 940 keV transition. In panel (c) several other lines are seen, and the $33/2^-_2\to 31/2^-_2\to 29/2^-_1$ and $33/2^-_2\to 31/2^-_2\to 29/2^-_2$ cascades are represented by the 1754 and 1660 keV and 1754 and 1388 keV lines, respectively. The amount of statistics in the data set is reflected in the obvious coincidences between transitions having very small relative intensities. For example, the coincidences between the 940 keV transition $(I_{rel}\sim 0.4\%)$ and the $33/2^-_2\to 29/2^-_4$ 2489 keV transition or the $33/2^-_2\to 29/2^-_3$ 2741 keV transition, both having $I_{rel}\sim 0.1\%$, are clear.

Not all of the core-excited states are connected to the yrast $27/2^-$ state, exemplified in panels (d) and (e). Panel (d) is the spectrum in coincidence with the $25/2^-_1\to 23/2^-_1$ 1421 keV transition. All other transitions in the low-energy yrast structure are present except for the $27/2^-_1\to 23/2^-_1$ 704 keV transition. In the high-energy portion of Fig. 4(d) four peaks are seen at 2913, 3169, 3311, and 3778 keV, which exclusively represent decays of nonyrast $27/2^-$ states. Figure 4(e) is the spectrum in coincidence with the $23/2^-_4\to 19/2^-_1$ 4283 keV transition. Only transitions below the yrast $19/2^-$ state are visible, as well as a line at 2376 keV, which forms the connection to the 10804 keV $27/2^-_3$ state.

On the right-hand side of Fig. 1 an isolated structure comprising states at 8085, 9471, 12981, and 13468 keV excitation energy is seen. Despite the relative strength of the 2295 keV transition the classification of these states is not straightforward. DCO ratios of 1.09(7), 1.12(6), and 1.14(7) for the three angle combinations, respectively, and $R_{30-83}=1.42(7)$ for the 2295 keV transition, are consistent with several spin assignments of the 9471 keV state. While an $I=29/2$ or $I=31/2$ assignment for this state is ruled out from yrast considerations, $I=23/2$, $I=25/2$, and $I=27/2$ assignments are in principle possible. Assuming negative parity for the 9471 keV state, an $I=23/2$ assignment is unlikely, since an angular distribution analysis of the 2295 keV transition gives a mixing ratio of 0.14. The same analysis for $I=25/2$ and $I=27/2$ assumptions reveals mixing ratios of 0.47 and a broad minimum around zero, respectively. Assuming a positive parity, an $I=25/2$ assignment is in principle ruled out due to the large mixing ratio, whereas an $I=23/2$ assignment

TABLE I. The energies of excited states in ^{51}Mn, the transition energies and relative intensities of the γ rays placed in the level scheme, the angular distribution ratios, the DCO ratios of three different angle combinations, and the spins and parities of the initial and final states of the γ rays.

E_x (keV)	E_γ (keV)	I_{rel} (%)	R_{30-83}	R_{DCO} 30°–53°	R_{DCO} 30°–83°	R_{DCO} 53°–83°	Mult. Ass.	I_i^π ($\hbar$)	I_f^π ($\hbar$)
237.4(4)	237.4(3)	99.1(30)	0.68(3)	0.86(4)	0.55(2)	0.64(3)	$E2/M1$	$7/2^-$	$5/2^-$
1139.8(4)	902.4(4)	47.7(14)	0.90(3)	0.84(4)	0.68(3)	0.68(4)	$E2/M1$	$9/2^-$	$7/2^-$
	1139.7(5)	4.5(2)	1.25(4)	0.84(7)	0.86(14)	0.92(7)	$E2$	$9/2^-$	$5/2^-$
1488.5(5)	348.8(3)	29.1(9)	0.66(3)	0.83(4)	0.55(3)	0.67(3)	$E2/M1$	$11/2^-$	$9/2^-$
	1251.1(6)	52.8(16)	0.95(3)	0.97(5)	0.80(4)	0.79(4)	$E2$	$11/2^-$	$7/2^-$
2957.3(6)	1468.8(7)	43.9(14)	0.90(3)	1.00(5)	0.78(3)	0.75(4)	$E2/M1$	$13/2^-$	$11/2^-$
	1817.5(8)	23.0(7)	0.92(3)	0.74(4)	0.74(4)	0.87(5)	$E2$	$13/2^-$	$9/2^-$
3250.8(6)	293.5(3)	2.9(1)	0.56(2)	0.83(15)	0.41(8)	0.68(6)	$E2/M1$	$15/2^-$	$13/2^-$
	1762.2(8)	39.1(12)	1.05(4)	0.80(5)	0.79(4)	0.82(5)	$E2$	$15/2^-$	$11/2^-$
3680.6(7)	430.1(3)	34.7(11)	0.52(2)	0.73(4)	0.40(2)	0.59(3)	$E2/M1$	$17/2^-$	$15/2^-$
	723.2(4)	59.7(18)	0.95(4)	0.78(4)	0.78(3)	0.84(4)	$E2$	$17/2^-$	$13/2^-$
4139.7(7)	459.2(2)	100.0(30)	0.66(3)	0.73(4)	0.52(2)	0.69(3)	$E2/M1$	$19/2^-$	$17/2^-$
	888.4(5)	0.9(1)					$E2$	$19/2^-$	$15/2^-$
5258.4(19)	1577(2)	0.2(1)					$\Delta I=0,1$	$17/2;19/2$	$17/2^-$
5458.4(11)	1318(1)	0.8(2)					$\Delta I=0$	$19/2^-$	$19/2^-$
	2207.7(12)	1.6(2)	1.70(15)				$E2$	$19/2^-$	$15/2^-$
5640.0(8)	1500.0(6)	86.5(26)	0.54(2)	0.63(3)	0.44(2)	0.65(3)	$E2/M1$	$21/2^-$	$19/2^-$
	1959.3(7)	1.2(1)	1.23(4)	1.19(21)	0.95(23)	1.04(16)	$E2$	$21/2^-$	$17/2^-$
6471.4(8)	831.8(4)	72.3(22)	0.65(3)	0.72(4)	0.51(2)	0.68(3)	$E2/M1$	$23/2^-$	$21/2^-$
	1012(1)	0.2(1)					$E2$	$23/2^-$	$19/2^-$
	2332.0(8)	16.7(5)	1.34(5)	0.94(5)	1.01(5)	1.01(5)	$E2$	$23/2^-$	$19/2^-$
6822.5(10)	2683.6(9)	1.8(3)	0.42(3)	0.54(18)	0.29(8)	0.44(9)	$E2/M1$	$21/2^-$	$19/2^-$
7176.0(9)	704.4(4)	65.1(20)	1.28(5)	0.98(5)	0.95(4)	1.01(5)	$E2$	$27/2^-$	$23/2^-$
7499.6(10)	2045(2)	0.2(1)					$E2/M1;E2$	$21/2^-;23/2^-$	$19/2^-$
	3361(2)	0.2(1)					$E2/M1;E2$	$21/2^-;23/2^-$	$19/2^-$
7666.7(9)	1195.4(6)	0.5(1)					$\Delta I=0$	$23/2^-$	$23/2^-$
	2026.6(7)	1.4(3)	0.44(3)				$E2/M1$	$23/2^-$	$21/2^-$
	2208(1)	0.3(1)					$E2$	$23/2^-$	$19/2^-$
7892.4(9)	716.8(6)	4.4(2)					$E2/M1$	$25/2^-$	$27/2^-$
	1420.9(6)	7.9(3)	0.61(2)	0.76(10)	0.33(4)	0.58(6)	$E2/M1$	$25/2^-$	$23/2^-$
	2251.8(10)	0.4(2)					$E2$	$25/2^-$	$21/2^-$
8084.7(9)	1612.8(5)	2.2(2)	1.49(9)	0.65(14)	0.94(13)	1.08(16)	$\Delta I=0,1$	$21/2^-;23/2$	$23/2^-$
	2446.0(10)	0.3(1)	0.88(14)				$\Delta I=0,1$	$21/2^-;23/2$	$21/2^-$
8415.4(20)	1119(2)	0.1(1)					$(E2)$	$(19/2^+)$	$(15/2^+)$
	3155(3)	0.2(1)					$\Delta I=1$	$(19/2^+)$	$(17/2)$
8424.0(20)	4283(2)	0.6(2)	1.69(26)				$E2$	$23/2^-$	$19/2^-$
8973.0(10)	1307.0(10)	0.3(1)					$E2/M1$	$25/2^-$	$23/2^-$
	1795(2)	0.2(1)					$E2/M1$	$25/2^-$	$27/2^-$
	2150.4(10)	0.2(1)					$E2$	$25/2^-$	$21/2^-$
	2501.8(10)	1.9(2)	0.47(4)	0.70(19)	0.49(13)	0.73(14)	$E2/M1$	$25/2^-$	$23/2^-$
	3331.3(16)	0.3(1)	1.74(35)				$E2$	$25/2^-$	$21/2^-$
9165.3(14)	1301(2)	<0.1					$(E2)$	$(21/2^+)$	$(17/2^+)$
	5024(4)	0.1(1)					$(E1)$	$(21/2^+)$	$19/2^-$
9471.0(10)	1386.1(5)	1.2(2)	1.34(10)				$\Delta I=2$	$25/2^-;27/2$	$21/2^-;23/2$
	1579.9(6)	0.3(1)	0.99(16)				$\Delta I=0,1$	$25/2^-;27/2$	$25/2^-$
	2294.7(10)	4.9(3)	1.42(7)	1.09(7)	1.12(6)	1.14(7)	$\Delta I=0,1$	$25/2^-;27/2$	$27/2^-$

TABLE I. (*Continued.*)

E_x (keV)	E_γ (keV)	I_{rel} (%)	R_{30-83}	R_{DCO} 30°–53°	R_{DCO} 30°–83°	R_{DCO} 53°–83°	Mult. Ass.	I_i^π ($\hbar$)	I_f^π ($\hbar$)
9599.9(11)	1175(1)	<0.1					$E2/M1$	$25/2^-$	$23/2^-$
	2100(1)	0.3(1)	0.94(24)				$E2;E2/M1$	$25/2^-$	$21/2^-$; $23/2^-$
	2423.8(10)	0.5(2)	0.66(11)				$E2/M1$	$25/2^-$	$27/2^-$
	2776(2)	0.2(1)					$E2$	$25/2^-$	$21/2^-$
	3133(2)	0.3(1)	1.64(18)				$E2/M1$	$25/2^-$	$23/2^-$
	3955(3)	0.2(1)					$E2$	$25/2^-$	$21/2^-$
9676.1(13)	2853.5(11)	0.3(1)	1.56(12)				$E2$	$25/2^-$	$21/2^-$
	4038(3)	0.6(2)	1.49(9)				$E2$	$25/2^-$	$21/2^-$
9919.3(14)	3450(2)	0.6(2)	1.38(16)				$E2/M1$	$25/2^-$	$23/2^-$
9979.3(12)	814(1)	0.1(1)					$(E2/M1)$	$23/2^{(+)}$	$(21/2^+)$
	1563(2)	0.2(1)					$(E2)$	$23/2^{(+)}$	$(19/2^+)$
	3158.3(12)	0.4(1)	0.65(7)	0.29(9)	0.62(8)	0.65(10)	$(E1)$	$23/2^{(+)}$	$21/2^-$
	3505(3)	0.1(1)					$\Delta I=0$	$23/2^{(+)}$	$23/2^-$
10468.6(11)	3293.5(12)	0.7(2)	0.79(7)	0.68(10)	0.79(9)	0.84(10)	$\Delta I=0$	$27/2^-$	$27/2^-$
	3998(2)	0.7(2)	1.96(52)				$E2$	$27/2^-$	$23/2^-$
10804.3(11)	1125(2)	0.1(1)					$E2/M1$	$27/2^-$	$25/2^-$
	1831(3)	0.2(1)					$E2/M1$	$27/2^-$	$25/2^-$
	2376(3)	0.1(1)					$E2$	$27/2^-$	$23/2^-$
	2912.7(10)	1.0(2)	0.42(5)	0.26(18)	0.53(14)	0.36(13)	$E2/M1$	$27/2^-$	$25/2^-$
	3628(3)	0.1(1)					$\Delta I=0$	$27/2^-$	$27/2^-$
10843.4(12)	862(2)	0.2(1)					$(E2/M1)$	$25/2^{(+)}$	$23/2^{(+)}$
	1678(2)	0.2(1)					$(E2)$	$25/2^{(+)}$	$(21/2^+)$
	4369.9(15)	0.5(1)	0.80(6)				$(E1)$	$25/2^{(+)}$	$23/2^-$
11062.1(12)	2089(2)	0.2(1)					$E2/M1$	$27/2^-$	$25/2^-$
	3169.2(11)	0.6(2)	0.93(11)				$E2/M1$	$27/2^-$	$25/2^-$
11201.0(15)	1282(1)	0.1(1)					$(E2/M1)$	$(27/2)^-$	$25/2^-$
	3311(3)	0.2(1)					$(E2/M1)$	$(27/2)^-$	$25/2^-$
	3532(2)	0.2(1)	1.32(36)				$(E2)$	$(27/2)^-$	$23/2^-$
11509.9(11)	4336.4(15)	4.3(4)	1.65(8)	1.21(9)	1.21(9)	1.04(8)	$E2/M1$	$29/2^-$	$27/2^-$
11671.4(15)	3778.4(12)	0.3(1)	0.54(10)				$E2/M1$	$27/2^-$	$25/2^-$
11781.1(11)	1312.3(7)	0.3(1)	0.85(12)				$E2/M1$	$29/2^-$	$27/2^-$
	2808(2)	0.3(1)					$E2$	$29/2^-$	$25/2^-$
	4605.8(15)	3.3(4)	0.44(3)	0.52(7)	0.32(3)	0.52(5)	$E2/M1$	$29/2^-$	$27/2^-$
11946.0(11)	1102.3(5)	0.2(1)	1.27(13)				$(E2/M1)$	$27/2^{(+)}$	$25/2^{(+)}$
	1967.3(8)	0.6(1)	1.59(12)	0.96(15)	1.07(13)	0.81(12)	$E2$	$27/2^{(+)}$	$23/2^{(+)}$
	2271(2)	<0.1					$(E1)$	$27/2^{(+)}$	$25/2^-$
	2972(2)	0.1(1)					$(E1)$	$27/2^{(+)}$	$25/2^-$
	4053(4)	<0.1					$(E1)$	$27/2^{(+)}$	$25/2^-$
	4777(4)	<0.1					$\Delta I=0$	$27/2^{(+)}$	$27/2^-$
12184.8(12)	1122(3)	0.1(1)	0.61(11)				$E2/M1$	$29/2^-$	$27/2^-$
	1376(2)	0.2(1)					$E2/M1$	$29/2^-$	$27/2^-$
	1717.0(10)	0.3(1)	0.41(9)				$E2/M1$	$29/2^-$	$27/2^-$
	2268(2)	<0.1					$E2$	$29/2^-$	$25/2^-$
	2585(2)	0.6(2)	1.59(33)				$E2$	$29/2^-$	$25/2^-$
	5009.8(17)	1.5(3)	0.66(4)	0.92(15)	0.46(6)	0.61(8)	$E2/M1$	$29/2^-$	$27/2^-$
12433.3(11)	1630(1)	0.3(1)	1.10(23)				$E2/M1$	$29/2^-$	$27/2^-$
	2512(2)	0.1(1)					$E2$	$29/2^-$	$25/2^-$
	3460(3)	0.1(1)					$E2$	$29/2^-$	$25/2^-$

TABLE I. (*Continued.*)

E_x (keV)	E_γ (keV)	I_{rel} (%)	R_{30-83}	$R_{\rm DCO}$ 30°–53°	$R_{\rm DCO}$ 30°–83°	$R_{\rm DCO}$ 53°–83°	Mult. Ass.	I_i^π ($\hbar$)	I_f^π ($\hbar$)
	5257.8(17)	1.5(3)	0.60(4)	1.04(22)	0.65(8)	0.70(9)	$E2/M1$	$29/2^-$	$27/2^-$
12791.4(11)	1010.0(5)	0.2(1)	1.20(22)				$E2/M1$	$31/2^-$	$29/2^-$
	5617.2(18)	5.8(6)	1.54(7)	1.12(8)	1.21(8)	1.16(8)	$E2$	$31/2^-$	$27/2^-$
12890.8(18)	3420.4(15)	0.3(1)	0.47(10)				$\Delta I=1$	$27/2^-;29/2$	$25/2^-;27/2$
13169.5(11)	1388.0(7)	0.2(1)	0.84(18)				$E2/M1$	$31/2^-$	$29/2^-$
	1659.6(6)	0.5(2)	1.03(12)	1.20(57)	0.90(13)	0.83(15)	$E2/M1$	$31/2^-$	$29/2^-$
	2701(3)	0.1(1)					$E2$	$31/2^-$	$27/2^-$
	5995.6(20)	1.4(3)	1.63(10)	1.37(23)	1.36(18)	1.06(17)	$E2$	$31/2^-$	$27/2^-$
13467.7(19)	3996.7(15)	0.9(2)	1.33(15)				$\Delta I=2$	$29/2^-;31/2$	$25/2^-;27/2$
13584.8(11)	1151.7(6)	0.2(1)	0.92(17)				$E2/M1$	$31/2^-$	$29/2^-$
	2075.0(6)	0.2(1)	0.34(8)	0.85(21)	0.48(9)	0.47(9)	$E2/M1$	$31/2^-$	$29/2^-$
	2522(1)	0.2(1)					$E2$	$31/2^-$	$27/2^-$
	2780(2)	0.2(1)					$E2$	$31/2^-$	$27/2^-$
13963.3(11)	1171.8(5)	2.8(2)	0.75(5)	0.75(5)	0.51(4)	0.59(5)	$E2/M1$	$33/2^-$	$31/2^-$
	2182.4(9)	0.2(1)					$E2$	$33/2^-$	$29/2^-$
	2453.2(10)	0.2(1)	1.28(19)				$E2$	$33/2^-$	$29/2^-$
14125.1(17)	2350(2)	0.2(1)					$E2/M1$	$31/2^-$	$29/2^-$
	2451(2)	<0.1					$E2$	$31/2^-$	$27/2^-$
	6944.1(26)	0.1(1)	2.01(44)				$E2$	$31/2^-$	$27/2^-$
14318.2(16)	2372.2(11)	0.9(2)	1.37(10)	0.93(15)	0.97(10)	0.69(11)	$E2$	$31/2^{(+)}$	$27/2^{(+)}$
14923.8(12)	1340.0(10)	0.3(1)	0.60(8)				$E2/M1$	$33/2^-$	$31/2^-$
	1754(1)	0.2(1)					$E2/M1$	$33/2^-$	$31/2^-$
	2489.4(14)	0.1(1)					$E2$	$33/2^-$	$29/2^-$
	2741(2)	0.1(1)					$E2$	$33/2^-$	$29/2^-$
	3144(3)	0.1(1)	1.77(56)				$E2$	$33/2^-$	$29/2^-$
	3417(3)	0.1(1)					$E2$	$33/2^-$	$29/2^-$
15388.2(25)	2217(3)	0.2(1)	0.94(39)				$\Delta I=0$; $E2/M1$	$31/2$; $33/2^-$	$31/2^-$
	3876(3)	<0.1					$(E2)$	$(33/2)^-$	$29/2^-$
15862.1(13)	939.5(10)	0.4(1)	1.37(19)				$(E2/M1)$	$(35/2)^-$	$33/2^-$
	1898.0(10)	0.1(1)					$(E2/M1)$	$(35/2)^-$	$33/2^-$
	2275(2)	0.1(1)					$(E2)$	$(35/2)^-$	$31/2^-$
	3071(2)	0.1(1)	1.88(71)				$(E2)$	$(35/2)^-$	$31/2^-$
17061.8(20)	2743.6(11)	0.4(1)	1.42(14)	1.27(26)	1.16(16)	0.82(16)	$E2$	$35/2^{(+)}$	$31/2^{(+)}$
19635.8(28)	2574(2)	0.2(1)	1.64(25)				$E2$	$39/2^{(+)}$	$35/2^{(+)}$

is unlikely, since a lifetime in the nanosecond regime would be expected. As discussed below, this is not the case.

It is interesting to note that the 1386, 1612, and 2295 keV transitions are the only transitions, except the transitions below the yrast $27/2^-$ state, which show a stopped component in the backed data. This indicates a lifetime $\tau \gtrsim 1$ ps for the 9471 keV state, which is significantly different from all other core-excited states.

Three other levels have ambigous spin-parity assignments: (1) The 5258 keV level can have spin $17/2$ or $19/2$ with unknown parity. Based on yrast arguments, a $17/2$ assignment is considered more likely. (2) The 7500 keV level must have $I^\pi = 21/2^-$ or $23/2^-$. Since the R_{30-83} ratio of the populating 2100 keV transition has a rather large uncertainty, it is not possible to fix the spin of the 7500 keV state. (3) The 15388 keV state can have $I = 31/2$ or $I^\pi = 33/2^-$. The latter assignment, however, is preferred due to yrast arguments and the decay pattern.

IV. SHELL-MODEL INTERPRETATION

To interpret the excited negative-parity states in ^{51}Mn, large-scale shell-model calculations were performed using the shell-model code ANTOINE [34,35]. The calculations were performed using the KB3G interaction [36] in the full fp space containing the $1f_{7/2}$ orbit below, and the $2p_{3/2}$, $1f_{5/2}$, and $2p_{1/2}$ orbits above the $N,Z=28$ shell closure. The configuration space was truncated to only allow for five particle

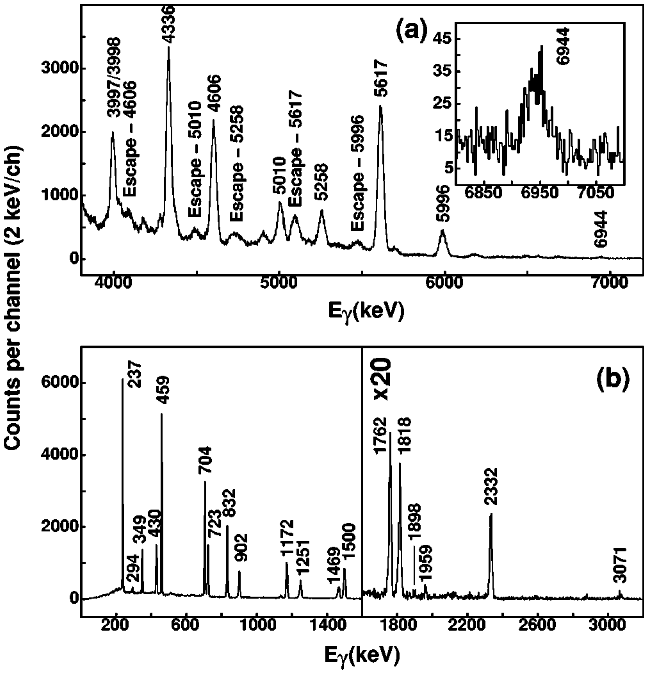

FIG. 2. Panel (a) shows the high-energy region of a sum spectrum in coincidence with several strong transitions below the yrast $27/2^-$ state from a $\gamma\gamma$ matrix gated by two α particles and one proton. Panel (b) shows a spectrum in coincidence with the 5617 keV transition from the same $\gamma\gamma$ matrix.

excitations from the $1f_{7/2}$ shell to the upper fp shell. Calculations performed on the $1f_{7/2}$ yrast structure in ^{51}Mn using this configuration space have been shown to give results more or less indistinguishable from calculations performed in the full fp configuration space [36]. In the calculations, bare g factors and effective charges of $1.5e$ for protons and $0.5e$ for neutrons were used. Experimental γ-ray energies were used to calculate branching and mixing ratios of transitions and lifetimes of nuclear states.

The results of the calculations are summarized in Figs. 5–7 and in Table II. On the left-hand side of Fig. 5(a) the calculated energy eigenvalues are compared with observed excitation energies for the yrast structure up to spin $I=27/2$. The overall agreement is very good and the comparison yields an expected small mean level deviation (MLD) of 113 keV and a binding-energy shift (BES) of −134 keV. The latter has been added to all calculated levels in Fig. 5. The BES is chosen to minimize the MLD and to quantatively compare the MLD of states at different excitation energies, while theoretical implications on the employed effective interaction based on BES values lie outside the scope of the present paper.

In Table II electromagnetic properties are compared, and the agreement between experimental and calculated branching ratios for the previously known yrast sequence is striking and reflected in a mean branching deviation (MBD) [37] smaller than 0.05. Minor exceptions are the $13/2^-$, $17/2^-$, and $23/2^-$ states. The reduced transition probabilities for the 430 and 723 keV transitions depopulating the yrast $17/2^-$ state are all very small, and thus they represent extremely subtle probes of the wave functions. For example, the calculated and experimental $B(E2;17/2^-\rightarrow 13/2^-)$ values are 0.184 and 0.11(1) W.u. (W.u.=Weisskopf unit), respectively. As a consequence the predicted lifetime of the $17/2^-$ state is almost a factor of 2 smaller than what is experimentally observed.

In all other yrast states the observed mixing ratios and lifetimes, where available, are well reproduced. For example, the calculated and experimental lifetime of the $9/2^-$ state are 0.55 and $0.36\left(^{11}_{8}\right)$ ps, respectively, and the predicted and experimental mixing ratio, $\delta(E2/M1)$, for the 902 keV $9/2^- \rightarrow 7/2^-$ transition are identical.

The inversion of the yrast $25/2^-$ and $27/2^-$ states is a result of the extra binding from one $1f_{7/2}$ neutron and one $1f_{7/2}$ proton coupled to $I=7$ in the latter. The 101(4) ps lifetime of the $27/2^-$ state is a result of this inversion and the relatively low energy (704 keV) of the $27/2^-_1 \rightarrow 23/2^-_1$ tran-

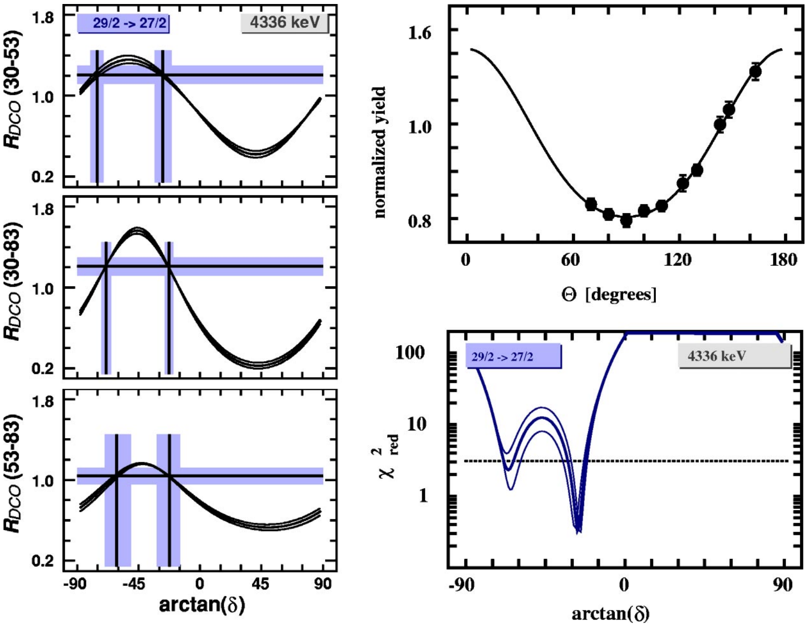

FIG. 3. (Color online) The left panel shows the analysis of DCO ratios for different detector angle combinations for the 4336 keV $29/2^- \rightarrow 27/2^-$ transition. The horizontal line is the experimental DCO ratio with error margin indicated in gray. The solid curves are the theoretical DCO ratio for the alignment coefficients $\alpha_2=0.80(5)$ for the initial state and the experimental value 0.57(4) for the final state. The crossings of the curve with the experimental DCO ratio mark possible solutions for the mixing ratio, indicated by the vertical solid lines. Again, the error margin is indicated in gray. Taking the weighted mean of the three angle combinations gives the solutions $\delta_1=-2.29\left(^{35}_{45}\right)$ and $\delta_2=-0.51\left(^{7}_{9}\right)$. The right panel shows the angular distribution of the same transition (top figure) with the associated reduced X^2 analysis. The solution are $\delta_1=-2.2(6)$ and $\delta_2=-0.51\left(^{11}_{16}\right)$.

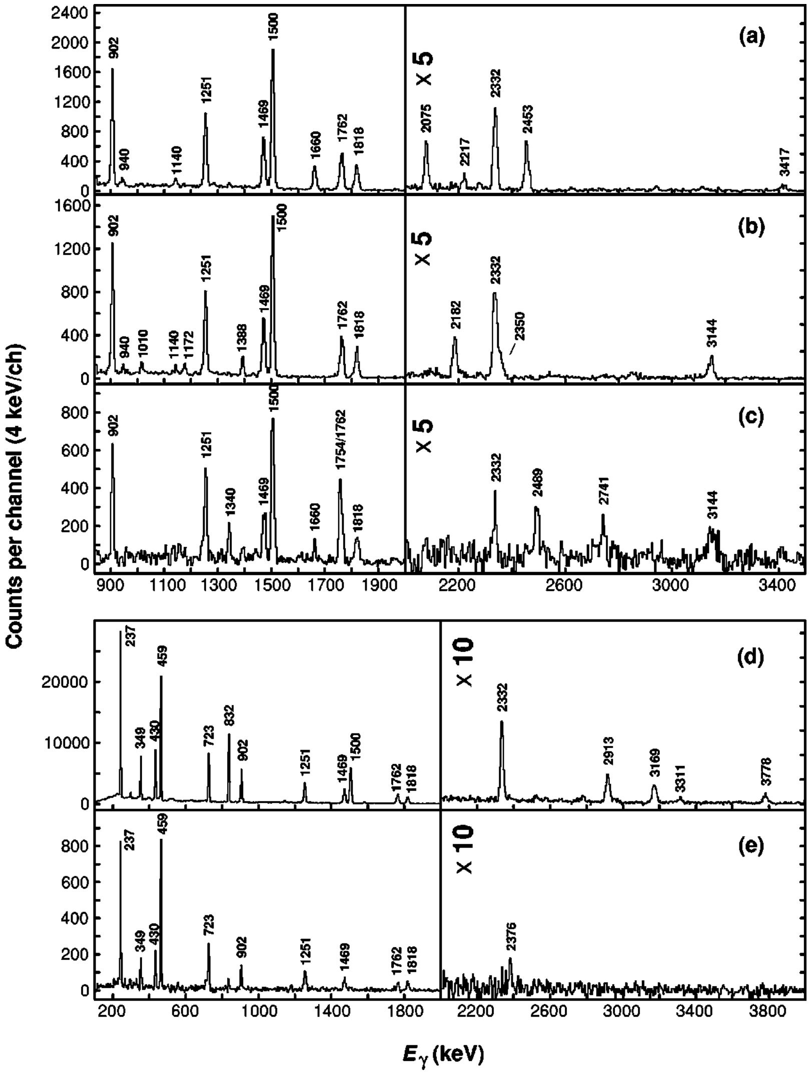

FIG. 4. Gamma-ray spectra of ^{51}Mn are shown deduced from a $\gamma\gamma$ matrix gated by two α particles and one proton, or two α particles and the strong transitions below the yrast $27/2^-$ state. Panel (a) shows the spectrum in coincidence with the $29/2_1^- \rightarrow 27/2_1^-$ 4336 keV transition, (b) in coincidence with the $29/2_2^- \rightarrow 27/2_1^-$ 4606 keV transition, (c) in coincidence with the $35/2_1^- \rightarrow 33/2_2^-$ 940 keV transition, (d) in coincidence with the $25/2_1^- \rightarrow 23/2_1^-$ 1421 keV transition, and (e) in coincidence with the $23/2_4^- \rightarrow 19/2_1^-$ 4283 keV transition.

sition. The experimental $B(E2)$ value is 4.12(13) W.u., indicating that no structural hindrance in the transition is present. It is also seen in Table II that all predicted lifetimes in the yrast structure, except for the $7/2^-$, $17/2^-$, and $27/2^-$ states, are small.

Figure 6 shows the predicted average $2p_{1/2}$, $2p_{3/2}$, and $1f_{5/2}$ particle occupancies as a function of angular momentum for the observed yrast sequence. All particle occupancies are on average decreasing with increasing angular momentum from the $5/2^-$ ground state up to the fully aligned $27/2^-$ state. This observation is consistent with a gradual decrease in deformation when the angular momentum increases, since excitations to the $2p_{3/2}$ orbit are expected to promote quadrupole deformation.

On the right-hand side of Fig. 5(a) the observed nonyrast $17/2^-$ to $23/2^-$ states, and in Fig. 5(b) the observed $25/2^-$ to $35/2^-$ states, are compared with the calculated level energies. The agreement for these states is good with MLD $=229$ keV and BES $=-80$ keV. The corresponding values for all observed states are MLD $=201$ keV and BES $=-92$ keV, respectively. However, to estimate the validity of the calculated wave functions one should compare the electromagnetic properties in Table II, rather than the excitation energies. Such a comparison yields MBD ~ 0.13 for the core-excited states and MBD ~ 0.10 for all states observed. Given that the MBD is calculated including states which are nonyrast by up to ~ 2 MeV, the resulting MBDs are remarkably good and imply that the previously unknown states in ^{51}Mn are generally well described in fp shell-model calculations. The association of experimental and calculated states follows the sequence in excitation energy, which is also justified when comparing calculated and experimental branching ratios.

However, the discrepancies between the calculated and experimental mixing ratios of the high-energy transitions depopulating the $29/2^-$ states indicate that the transition probabilities in these states are not perfectly reproduced. These discrepancies could possibly result from configurations including two particles in the $1g_{9/2}$ shell, which are not accounted for in the calculations.

To increase the spin beyond $I=27/2$ at least one particle must be promoted from the $1f_{7/2}$ orbit into the upper fp shell. As a consequence, the occupation numbers for these orbits are increasing, as seen in Fig. 6. The maximum spin that can be created when promoting one particle (neutron) to the upper fp shell is $I=35/2$. A detailed inspection of the calcu-

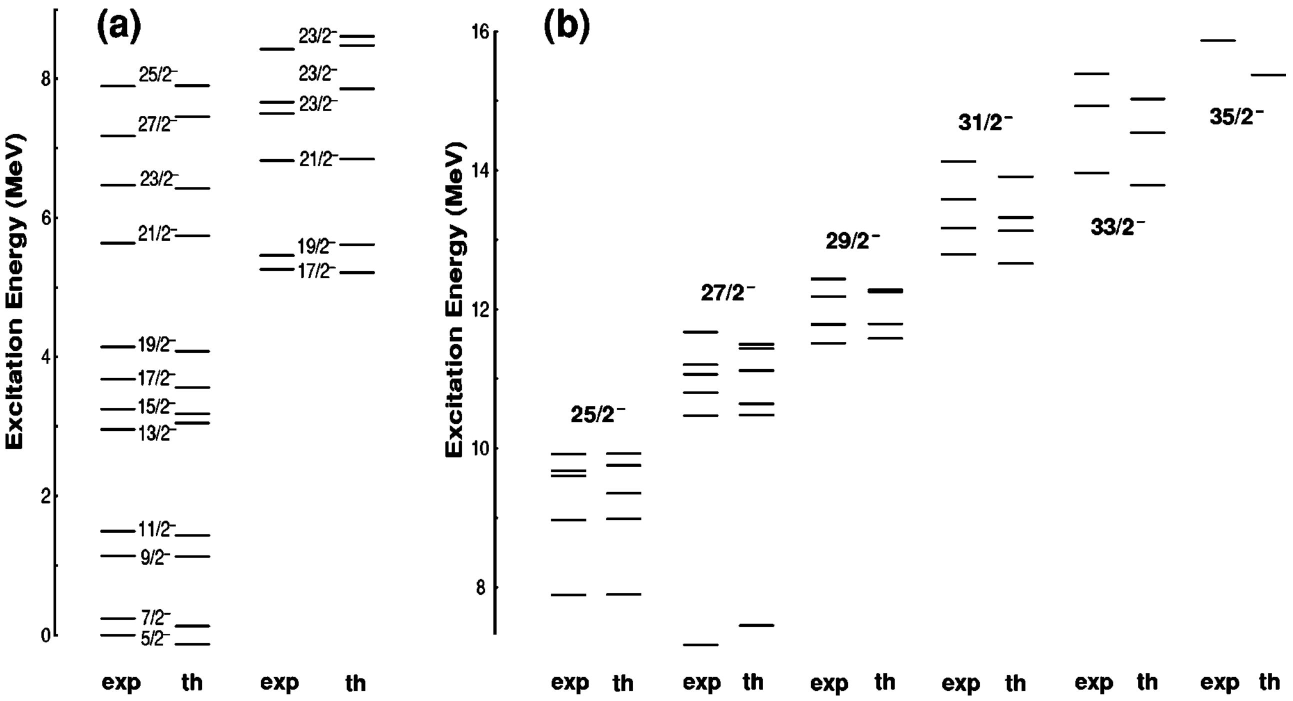

FIG. 5. Experimental and calculated excitation energies for the observed states between (a) $I^{\pi}=5/2^-$ and $27/2^-$ and (b) $I^{\pi}=25/2^-$ and $35/2^-$. For all calculated states a binding-energy shift of −134 keV has been added to the excitation energies.

lated wave functions reveals that the $[\pi(1f_{7/2})^{-3} \otimes \nu(1f_{7/2})^{-3}]_{15^+} \otimes \nu(1f_{5/2})$ configuration accounts for 80% of the yrast $35/2^-$ wave function. The leading configuration of the yrast $33/2^-$ state is obtained by replacing the $1f_{5/2}$ neutron with a $2p_{3/2}$ neutron. In Fig. 7 the average neutron and proton occupation numbers for the orbits in the upper *fp* shell are shown for the yrast and nonyrast $29/2^-$ and $31/2^-$ states. The yrast $29/2^-$ and $31/2^-$ states are built on a neutron in the $2p_{3/2}$ orbit, and a neutron in the $2p_{3/2}$ or $1f_{5/2}$ orbit, respectively. The dominance of these configurations in the yrast core-excited states can be understood qualitatively by studying the level schemes of ^{50}Mn and ^{50}Cr. Here it appears as if the coupling of one $2p_{3/2}$ or $1f_{5/2}$ neutron to the 13^+ and 15^+ states in ^{50}Mn is favored, compared to the coupling of a proton to the ^{50}Cr "core." From Fig. 7 it is seen that the $29/2^-_2$ state, to leading order, is formed by exciting either one proton or one neutron to the $1f_{5/2}$ orbit. The occupation numbers of the $29/2^-_3$ and $29/2^-_4$ states are somewhat unstable, since the two states are predicted to be separated by only 33 keV. Furthermore, it is seen that the $31/2^-_3$

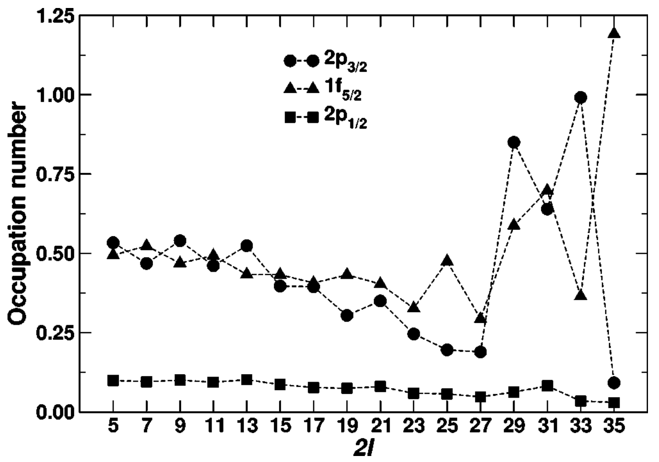

FIG. 6. Occupation numbers as a function of angular momentum for the negative-parity yrast sequence. Circles, triangles, and squares represent $2p_{3/2}$, $1f_{5/2}$, and $2p_{1/2}$ occupancies, respectively.

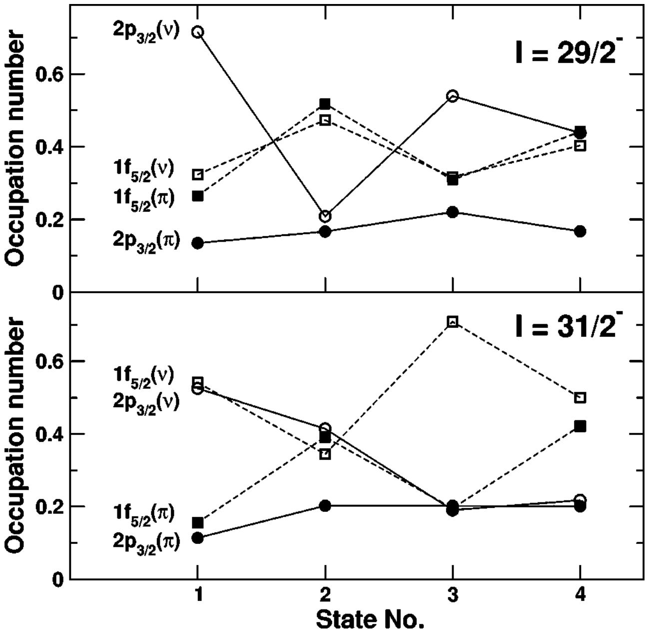

FIG. 7. Occupation numbers for the $29/2^-$ states (top) and $31/2^-$ states (bottom). Open (filled) circles represent $2p_{3/2}$ neutron (proton) occupancies and open (filled) squares represent $1f_{5/2}$ neutron (proton) occupancies.

TABLE II. Comparison of experimental branching ratios b of γ rays depopulating negative parity states in ^{51}Mn with predictions from shell-model calculations. The calculated mixing ratios δ and lifetimes τ are provided as well, and if information is available, compared to experimental values. Transitions which have not been observed, but could have been in terms of their predicted relative intensity, $I_{rel}>0.1$, have their energies given in italic numbers.

E_x (keV)	I_i ($\hbar$)	I_f ($\hbar$)	E_γ (keV)	b_{exp}	b_{theo}	δ_{exp}	δ_{theo}	τ_{exp} (ps)	τ_{theo} (ps)
237	7/2	5/2	237	1.00	1.00	−0.100(11)[a]	−0.08	20.4(33)[b]	24
1140	9/2	7/2	902	0.91(1)	0.89	−0.323(22)[a]	−0.32	$0.36(^{11}_{8})$[a]	0.55
		5/2	1140	0.09(1)	0.11				
1489	11/2	9/2	349	0.36(1)	0.35	−0.054(27)[a]	−0.06	$0.72(^{20}_{14})$[a]	1.1
		7/2	1251	0.64(1)	0.65				
2957	13/2	11/2	1469	0.66(1)	0.53		−0.42		0.13
		9/2	1818	0.34(1)	0.47				
3251	15/2	13/2	294	0.07(1)	0.08		−0.03		0.26
		11/2	1762	0.93(1)	0.92				
3681	17/2	15/2	430	0.37(1)	0.46		−0.03	$2070(^{80}_{70})$[c]	1100
		13/2	723	0.63(1)	0.54				
4140	19/2	17/2	459	0.99(1)	0.98	$0.15(^{6}_{5})$, $3.54(^{96}_{71})$	0.04		0.73
		15/2	888	0.01(1)	0.02				
5258	17/2	17/2	1577	1.00	0.10		0.24		0.026
5458	19/2	19/2	1318	0.33(7)	0.44		0.16		0.055
		15/2	2208	0.67(5)	0.43				
5640	21/2	19/2	1500	0.99(1)	0.98	$0.29(^{8}_{7})$, $2.09(^{50}_{49})$	0.13		0.020
		17/2	1959	0.01(1)	0.02				
6471	23/2	21/2	832	0.81(1)	0.72	$0.16(^{6}_{5})$, $3.42(^{103}_{68})$	0.04		0.054
		19/2	1012	0.00	0.00				
		19/2	2332	0.19(1)	0.27				
6823	21/2	19/2	2684	1.00	0.65		0.47		0.21
7176	27/2	23/2	704	1.00	1.00			101(4)[d]	86
7500	23/2	19/2	2045	0.50(21)	0.06				0.040
		19/2	3361	0.50(21)	0.14				
7667	23/2	23/2	1195	0.23(6)	0.01		0.23		0.089
		21/2	*844*	n.o.	0.20		−0.13		
		21/2	2027	0.64(7)	0.68		0.02		
		19/2	2208	0.14(5)	0.05				
7892	25/2	27/2	717	0.35(2)	0.36		0.00		0.042
		23/2	1421	0.62(1)	0.56		0.07		
	21/2	2252	0.03(1)	0.07					
8424	23/2	19/2	4283	1.00	0.85				0.028
8973	25/2	27/2	1795	0.07(4)	0.23		0.04		0.010
		23/2	1307	0.10(4)	0.00		0.93		
		23/2	*1473*	n.o.	0.16		0.08		
		23/2	2502	0.66(4)	0.42		0.11		
		21/2	2150	0.07(4)	0.06				
		21/2	3331	0.10(4)	0.10				
9600	25/2	27/2	2424	0.32(11)	0.10		0.15		0.016
		23/2	1175	0.03(3)	0.01		0.03		
		23/2	*1933*	n.o.	0.23		0.06		
		23/2	2100	0.19(7)	0.14		0.02		
		23/2	3133	0.19(7)	0.45		−0.24		
		21/2	2776	0.13(7)	0.00				

TABLE II. (*Continued.*)

E_x (keV)	I_i ($\hbar$)	I_f ($\hbar$)	E_γ (keV)	b_{exp}	b_{theo}	δ_{exp}	δ_{theo}	τ_{exp} (ps)	τ_{theo} (ps)
		21/2	3955	0.13(7)	0.05				
9676	25/2	21/2	2854	0.33(12)	0.17				0.020
		21/2	4038	0.67(11)	0.51				
9919	25/2	23/2	3450	1.00	0.60		3.04		0.029
10469	27/2	27/2	3294	0.50(11)	0.04		0.06		0.027
		23/2	*2800*	n.o.	0.67				
		23/2	3998	0.50(11)	0.01				
10804	27/2	27/2	3628	0.07(7)	0.05		−1.89		0.006
		25/2	1125	0.07(7)	0.01		0.26		
		25/2	1831	0.13(7)	0.27		0.05		
		25/2	2913	0.67(9)	0.17		−0.02		
		23/2	2376	0.07(7)	0.01				
		23/2	*4333*	n.o.	0.29				
11062	27/2	27/2	*3886*	n.o.	0.61		−6.74		0.011
		25/2	2089	0.25(13)	0.00		∞		
		25/2	3169	0.75(11)	0.26		0.48		
11201	27/2	25/2	1282	0.20(20)	0.08		0.10		0.017
		25/2	3311	0.40(19)	0.33		−0.21		
		23/2	3532	0.40(19)	0.02				
11510	29/2	27/2	4336	1.00	0.83	$-0.51\left(^{7}_{9}\right)$, $-2.29\left(^{35}_{45}\right)$	−1.00		0.016
11671	27/2	27/2	*4495*	n.o.	0.61		−1.10		0.009
		25/2	3778	1.00	0.08		4.64		
11781	29/2	27/2	1312	0.08(3)	0.00		0.04		0.003
		27/2	4606	0.85(2)	0.90	$0.35\left(^{11}_{8}\right)$, $2.05\left(^{51}_{49}\right)$	−0.19		
		25/2	2808	0.08(3)	0.06				
12185	29/2	27/2	1122	0.04(4)	0.02		0.04		0.004
		27/2	1376	0.07(4)	0.00		−0.66		
		27/2	1717	0.11(4)	0.02		0.19		
		27/2	5010	0.53(8)	0.91	$0.12\left(^{8}_{6}\right)$, $5.0\left(^{50}_{20}\right)$	−0.72		
		25/2	2268	0.02(2)	0.01				
		25/2	2585	0.21(7)	0.01				
		25/2	3212	0.04(4)	0.00				
12433	29/2	27/2	1630	0.15(6)	0.03		0.29		0.004
		27/2	5258	0.75(6)	0.83	$0.00\left(^{9}_{7}\right)$, $4.2\left(^{31}_{19}\right)$	0.21		
		25/2	2512	0.05(5)	0.03				
		25/2	3460	0.05(5)	0.00				
12791	31/2	29/2	1010	0.03(2)	0.11		−0.05		0.024
		27/2	*2322*	n.o.	0.07				
		27/2	5617	0.97(1)	0.80				
13170	31/2	29/2	1388	0.09(5)	0.01		0.37		0.010
		29/2	1660	0.23(9)	0.32		0.00		
		27/2	2701	0.05(5)	0.05				
		27/2	5996	0.64(8)	0.57				
13585	31/2	29/2	1152	0.25(12)	0.06		0.02		0.018
		29/2	2075	0.25(12)	0.06		0.55		
		27/2	2522	0.25(12)	0.00				
		27/2	2780	0.25(12)	0.21				

TABLE II. (*Continued.*)

E_x (keV)	I_i ($\hbar$)	I_f ($\hbar$)	E_γ (keV)	b_{exp}	b_{theo}	δ_{exp}	δ_{theo}	τ_{exp} (ps)	τ_{theo} (ps)
13963	33/2	31/2	1172	0.87(2)	0.65		−0.04		0.067
		29/2	2182	0.06(3)	0.01				
		29/2	2453	0.06(3)	0.33				
14125	31/2	29/2	2350	0.67(25)	0.20		0.08		0.016
		27/2	2451	0.14(14)	0.00				
		27/2	6944	0.33(33)	0.04				
14924	33/2	31/2	1340	0.33(12)	0.23		−0.07		0.028
		31/2	1754	0.22(12)	0.07		−0.63		
		29/2	2489	0.11(11)	0.03				
		29/2	2741	0.11(11)	0.13				
		29/2	3144	0.11(11)	0.37				
		29/2	3417	0.11(11)	0.11				
15388	33/2	31/2	2217	0.80(18)	0.62		0.06		0.010
		29/2	3876	0.20(20)	0.07				
15862	35/2	33/2	940	0.57(14)	0.43		−0.02		0.050
		33/2	1898	0.14(14)	0.01		$-\infty$		
		31/2	2275	0.14(14)	0.15				
		31/2	3071	0.14(14)	0.37				

[a] Taken from Ref. [19].
[b] Taken from Ref. [38].
[c] Taken from Ref. [13].
[d] Taken from Ref. [33].

state appears to have a rather pure $[\pi(1f_{7/2})^{-3} \otimes \nu(1f_{7/2})^{-3}]_{13^+} \otimes \nu(1f_{5/2})$ configuration, whereas the other nonyrast $31/2^-$ states are more mixed.

The previously mentioned structure on the right-hand side in Fig. 1 is not reproduced by the shell-model calculations, independently of what spin assignments are used, and it is therefore not included in Table II. This indicates that the main configurations of the states in the structure lie outside the model space used and likely include one or more $1g_{9/2}$ particles. This observation is supported by the fact that the structure is isolated from negative-parity nonyrast states and that the $\tau \gtrsim 1$ ps lifetime of the 9471 keV state is much longer than lifetimes of all other observed nonyrast states, indicating a structural hindrance in the 2295 keV transition. Assuming that the structure is based on one $1g_{9/2}$ particle, transitions connecting to the $1g_{9/2}$ rotational band [23] would eventually be expected, but the fact that the structure appears to be noncollective contradicts such an assignment. Another possibility is that two $1g_{9/2}$ particles are involved in the description of the states. Due to the extra binding of the two-body matrix element, a favored configuration could include a $1g_{9/2}$ neutron and a $1g_{9/2}$ proton coupled to spin $I=9$. Such configurations have been assigned to states in ^{58}Cu [18] and ^{59}Cu [32], but never for states in $1f_{7/2}$ nuclei. Based on the discussion above, it is tempting to assign a seniority $s=3$ $[(\pi 1g_{9/2} \otimes \nu 1g_{9/2})_{9^+} \otimes \nu 1f_{7/2}]$ configuration and thus $I^\pi = 25/2^-$ for the state at 9471 keV and a $[(\pi 1g_{9/2} \otimes \nu 1g_{9/2})_{7^+} \otimes \nu 1f_{7/2}]$ configuration and $I^\pi = 21/2^-$ for the state at 8085 keV. To increase the spin further, a $1f_{7/2}$ particle pair has to be broken and thus these states are expected to be a several MeV above the $25/2^-$ state. Indeed, candidates for such states exist at 12891 and 13468 keV. The spin and parity assignments suggested above are consistent with the experimental observations.

V. SUMMARY AND CONCLUSIONS

We have presented an extensive decay scheme of the odd-even nucleus ^{51}Mn comprising previously unknown core-excited states. A thorough and detailed comparison with large-scale shell-model calculations in the fp shell reveals an overall very good agreement, despite the fact that the model space used cannot account for configurations including particles in the $1g_{9/2}$ orbit. However, configurations including particles in the $1g_{9/2}$ orbit are present in the excitation scheme manifested by (i) a rotational band based on one neutron in the $1g_{9/2}$ orbit [23] and (ii) what appears to be a noncollective structure based on a $1g_{9/2}$ neutron and $1g_{9/2}$ proton pair.

ACKNOWLEDGMENTS

We would like to thank the accelerator crews and the Gammasphere support staff at Argonne and Berkeley for their supreme efforts. This work was supported in part by the Swedish Natural Science Research Councils and the U.S. Department of Energy under Grant Nos. DE-AC03-76SF00098 (LBNL), DE-FG05-88ER-40406 (WU), and W-31-109-ENG38 (ANL).

[1] T. Otsuka, M. Honma, and T. Mizusaki, Phys. Rev. Lett. **81**, 1588 (1998).
[2] F. Nowacki, Nucl. Phys. **A704**, 223c (2002).
[3] J.A. Cameron *et al.*, Phys. Rev. C **49**, 1347 (1994).
[4] S.M. Lenzi *et al.*, Z. Phys. A **354**, 117 (1996).
[5] F. Brandolini *et al.*, Nucl. Phys. **A642**, 387 (1998).
[6] A. Juodagalvis, I. Ragnarsson, and S. Åberg, Phys. Lett. B **477**, 66 (2000).
[7] M.A. Bentley *et al.*, Phys. Lett. B **437**, 243 (1998).
[8] C.D. O'Leary *et al.*, Phys. Rev. Lett. **79**, 4349 (1997).
[9] P.E. Garrett *et al.*, Phys. Rev. Lett. **87**, 132502 (2001).
[10] S.M. Lenzi *et al.*, Phys. Rev. Lett. **87**, 122501 (2001).
[11] C.D. O'Leary *et al.*, Phys. Lett. B **525**, 49 (2002).
[12] S.J. Williams *et al.*, Phys. Rev. C **68**, 011301 (2003).
[13] J. Ekman *et al.*, Eur. Phys. J. A **9**, 13 (2000).
[14] A. Poves and G. Martinez-Pinedo, Phys. Lett. B **430**, 203 (1998).
[15] J. Terasaki, R. Wyss, and P.-H. Hennen, Phys. Lett. B **437**, 1 (1998).
[16] A. Juodagalvis and S. Åberg, Phys. Lett. B **428**, 227 (1998).
[17] S.M. Lenzi *et al.*, Phys. Rev. C **56**, 1313 (1997).
[18] D. Rudolph *et al.*, Eur. Phys. J. A **4**, 115 (1999).
[19] J.W. Noé, R.W. Zurmühle, and D.P. Balamuth, Nucl. Phys. **A277**, 137 (1977).
[20] G. Fortuna, S. Lunardi, M. Morando, and C. Signorini, Nucl. Phys. **A299**, 479 (1978).
[21] J.A. Cameron *et al.*, Phys. Rev. C **44**, 2358 (1991).
[22] J.W. Noe and P. Gural, *International Conference on Medium-Light Nuclei*, edited by P. Blasi and R.A. Ricci (Florence, Italy, 1978), p. 459.
[23] J. Ekman *et al.*, Phys. Rev. C **66**, 051301 (2002).
[24] I.-Y. Lee, Nucl. Phys. **A520**, 641c (1990).
[25] M. Devlin *et al.*, Nucl. Instrum. Methods Phys. Res. A **383**, 506 (1996).
[26] D.G. Sarantites *et al.*, Nucl. Instrum. Methods Phys. Res. A **381**, 418 (1996).
[27] D.G. Sarantites *et al.*, Nucl. Instrum. Methods Phys. Res. A (in press).
[28] C. Andreiou, Ph.D. thesis, Lund University, 2002.
[29] D.C. Radford, Nucl. Instrum. Methods Phys. Res. A **386**, 297 (1995).
[30] J. Theuerkauf, S. Esser, S. Krink, M. Luig, N. Nicolay, O. Stuch, and H. Wolters, program TV, University of Cologne, Germany (unpublished).
[31] C.E. Svensson *et al.*, Nucl. Instrum. Methods Phys. Res. A **396**, 228 (1997).
[32] C. Andreiou *et al.*, Eur. Phys. J. A **14**, 317 (2002).
[33] R. du Rietz *et al.*, Phys. Rev. Lett. (submitted).
[34] E. Caurier, shell model code ANTOINE, IRES, Strasbourg, France, 1989–2002).
[35] E. Caurier and F. Nowacki, Acta Phys. Pol. B **30**, 705 (1999).
[36] A. Poves, J. Sánchez-Solano, E. Caurier, and F. Nowacki, Nucl. Phys. **A694**, 157 (2001).
[37] D. Rudolph, K.P. Lieb, and H. Grawe, Nucl. Phys. **A597**, 298 (1996).
[38] B.A. Brown, D.B. Fossan, J.M. McDonald, and K.A. Snover, Phys. Rev. C **9**, 1033 (1974).